Crystal-Facet Engineering of Ferric Giniite by Using Ionic-Liquid Precursors and Their Enhanced Photocatalytic Performances under Visible-Light Irradiation

Xiaochuan Duan, Di Li, Huili Zhang, Jianmin Ma, and Wenjun Zheng*[a]

Abstract: In the work presented here, well-dispersed ferric giniite microcrystals with controlled sizes and shapes are solvothermally synthesized from ionic-liquid precursors by using 1-*n*-butyl-3-methylimidazolium dihydrogenphosphate ([Bmim][H₂PO₄]) as phosphate source. The success of this synthesis relies on the concentration and composition of the ionic-liquid precursors. By adjusting the molar ratios of $Fe(NO_3)_3 \cdot 9H_2O$ to [Bmim][H₂PO₄] as well as the composition of ionic-liquid precursors, we obtained uniform microstructures such as bipyramids exposing {111} facets, plates exposing {001} facets, hollow spheres, tetragonal hexadecahedron exposing {441} and {111} facets, and truncated bipyamids with carved {001} facets. The crystalline structure of the ferric giniite microcrystals is disclosed by various characterization techniques. It was revealed that [Bmim][H₂PO₄] played an important role in stabilizing the {111} facets of ferric giniite crystals, leading to the different morphologies in the presence of ionic-liquid precursors with different compositions. Furthermore, since these ferric giniite crystals were characterized by different facets, they could serve as model Fenton-like catalysts to uncover the correlation between the surface and the catalytic performance for the photodegradation of organic dyes under visible-light irradiation. Our measurements indicate that the photocatalytic activity of as-prepared Fenton-like catalysts is highly dependent on the exposed facets, and the surface area has essentially no obvious effect on the photocatalytic degradation of organic dyes in the present study. It is highly expected that these findings are useful in understanding the photocatalytic activity of Fenton-like catalysts with different morphologies, and suggest a promising new strategy for crystal-facet engineering of photocatalysts for wastewater treatment based on heterogeneous Fenton-like process.

Keywords: crystal engineering · Fenton-like process · ferric giniite · oxidation · ionic liquids

Introduction

Generally, a heterogeneous photocatalytic reaction involves adsorption of reactant molecules on specific sites of catalysts, chemical transformation between photoexcited electrons and reactant molecules, and desorption of product molecules.[1–6] Considering that the above reaction processes take place on the surface of catalysts, surface atomic structures involving surface atomic arrangement and coordination play a critical role in determining the photocatalytic reactivity and efficiency. Since the surface atomic arrangement and coordination change with crystal facets in different orientations, crystal-facet engineering of catalysts has become an important strategy for fine-tuning the physicochemical properties and thus optimizing the reactivity and selectivity of photocatalysts.[7–12] It is conventionally considered that a high-energy facet with a high percentage of under-coordinated atoms possesses a superior reactivity to that with a low percentage of under-coordinated atoms, thus photocatalysts enclosed by high-index facets usually yields higher catalytic activity.[13–25] Recently, much interest has been focused on research into catalysts with morphologies that provide large percentages of highly reactive facets, which may represent a promising and efficient method for the further improvement of photocatalytic performance. One of the most important examples of facet-dependent photocatalytic activity is that reported by Lu and co-workers, who made a breakthrough in the synthesis of anatase TiO_2 with high-energy {001} facets, which have paved a new way for the enhancement of photocatalytic performance.[26] Now, it is no doubt that a large percentage of {001} facets has become a very popular target in the synthesis of anatase TiO_2 crystals.[27–31] For other facet-dependent photocatalysts, Ye and co-workers have developed a facile and general route for high-yield fabrication of single-crystalline Ag_3PO_4 rhombic dodecahedrons with only {110} facets exposed, and indicated that rhombic dodecahedrons exhibit much higher activities than cubes with {100} facets exposed.[32] Huang and co-workers have

[a] Dr. X. Duan, Dr. D. Li, Dr. H. Zhang, Dr. J. Ma, Prof. Dr. W. Zheng
Department of Materials Chemistry
Key Laboratory of Advanced Energy
Materials Chemistry (MOE)
and TKL of Metal and Molecule-Based
Material Chemistry, College of Chemistry
Nankai University, 94 Weijin Road
Tianjin, 300071 (P.R. China)
Fax: (+86) 022-23502458
E-mail: zhwj@nankai.edu.cn

Supporting information for this article is available on the WWW under http://dx.doi.org/10.1002/chem.201300385.

also found the Cu$_2$O rhombic dodecahedra exposing only the {110} facets exhibit an exceptionally good photocatalytic activity compared with cubes enclosed by {100} facets.[33] Similar conclusions could be verified by the photocatalytic performance of BiOX (X=Cl, Br, I) nanosheets with {001} facets exposed,[34–36] BiVO$_4$ sheets exposing {040} facets,[37] and so on. It should be noted that attempts to deliberately fabricate the catalysts enclosed by high-energy facets are challenged by the thermodynamic growth mechanisms of the crystals: high-energy facets usually grow fast and then vanish during the crystal growth, so most reported catalysts are of exposed low-energy facets. To address this issue, capping agents have been employed to selectively control the growth rates of planes of interest. However, the capping agents adsorbed on the surfaces of crystals during synthesis must be removed before they can be used in photocatalytic applications, often requiring complex treatments. Most importantly, the highly reactive facets may then lose many of their active sites as a result of surface reconstruction.[2] Therefore, it is still a great challenge to synthesize photocatalysts with exposed high-energy facets through a facile and environmentally friendly route.

The Fenton or Fenton-like reaction, as one of the most promising advanced oxidation processes (AOPs), has been reviewed by various researchers and its performance has been validated for different catalytic applications since it was first observed in 1894.[38–44] Based on highly aggressive hydroxyl radicals (OH$^{\cdot}$, E_o=2.80 V vs. the saturated calomel electrode (SHE)) generated from hydrogen peroxide through the catalytic reaction of Fe^{II}/Fe^{III}, the Fenton process can decompose a wide range and variety of organic pollutants, which are effectively oxidized or mineralized to CO$_2$ and H$_2$O. Unfortunately, the conventional Fenton process (homogeneous catalysis) has some drawbacks such as narrow working pH (2–3), iron sludge treatment, and deactivation of iron ions. In this context, there is considerable incentive in developing a heterogeneous Fenton-like process by using the catalysts with immobilized Fe^{III} species in the structure and in the pore/interlayer space. As a result, the catalyst can maintain its ability to generate hydroxyl radicals from hydrogen peroxide, and iron hydroxide precipitation is prevented. Correspondingly, in a large number of studies in the past few decades, these heterogeneous catalysts have demonstrated their usefulness in treating various organic pollutants in an aqueous environment.[45–50] However, it should be pointed out that the heterogeneous Fenton reaction itself is too slow, especially those containing Fe^{III} oxides, due to the slow reduction of Fe^{III} to Fe^{II} (k=0.001–0.1 M^{-1}S^{-1}).[51–52] Therefore, most heterogeneous Fenton catalysts are used in an aqueous environment with the assistance of UV irradiation for the acceleration of the reaction, resulting in the need for specific equipment at additional cost. In this respect, it is well-understood that significant attention has been directed towards using solar-driven heterogeneous Fenton catalysts with a high catalytic activity and long-term stability. Taking into account that crystal-facet engineering of catalysts has exhibited powerful improvements for photo-

catalytic performance, it is regrettable that far less information is available concerning the facet effects on the Fenton-like catalysts. Most recently, Zhi and co-workers investigated the facet-dependent photo-Fenton-like catalytic performance by using hematite as the model, and demonstrated that the photodegradation of rhodamine B was highly determined by the exposed facets.[53] We believe that facet engineering proposes a promising new strategy of rational design and synthesis of heterogeneous Fenton catalysts for wastewater treatment.

In this study, we report a facile one-pot approach employing ionic-liquid precursors, which permit exquisite control over the morphology of Fe$_5$(PO$_4$)$_4$(OH)$_3$·2H$_2$O (ferric giniite) microstructures without templates or surfactants in the reaction system. By adjusting the molar ratios of Fe(NO$_3$)$_3$·9H$_2$O to [Bmim][H$_2$PO$_4$] as well as the composition of ionic-liquid precursors, monodispersed and high crystalline ferric giniite microstructures with controlled morphologies can be obtained, which are named bipyramid (S-1), plate (S-2), hollow sphere (S-3), tetragonal hexadecahedron (S-4), and carved bipyramid (S-6). Our experimental results demonstrate that the ionic-liquid precursor plays a key role of forming different shapes of ferric giniite microstructures that expose different facets. The mechanism for the formation of ferric giniite crystals was proposed on the basis of the characterization results. There are three significant features in this work: 1) Although great efforts have been made on the synthesis of inorganic materials by using the ionothermal synthesis or ionic liquid-assisted synthesis, which is widely considered to be a "green" synthetic route, the synthesis of metal phosphates by using ionic liquids (ILs) has been rarely studied.[54–57] Moreover, it seems that little work has been focused on the designability of ILs; it is reasonable to conceive that ILs with special cations and anions can be tailored according to the composition, initial crystalline structure, and crystal-growth habit of the material, to purposefully synthesize inorganic nanomaterials with new morphologies and improved properties.[58–77] It is not enough to just simply exhibit the advantages of ILs as a soft template or a capping agent. Herein, we report our recent finding that [Bmim][H$_2$PO$_4$] may represent a new phosphate precursor and show how we can successfully employ it to prepare ferric giniite microstructures with controllable shapes and conclude the following key points: 1) Specifically, the tetragonal hexadecahedron enclosed by {441} and {111} facets is a shape rarely observed for nanocrystals; 2) The photocatalytic performances of the as-prepared ferric giniite microstructures as the Fenton-like catalysts have also been researched. Compared with the traditional photo-Fenton-like process that requires the assistance of UV irradiation, the as-prepared ferric giniite microstructures provides more possibility to serve as an ideal Fenton-like catalyst under visible-light irradiation. It is highly expected that such a simple and mild route could also to be extended to prepare other natural, abundant, inexpensive and environmentally friendly photocatalysts. 3) In contrast to numerous researches in the past that sought catalysts with small parti-

cle sizes to increase the catalytic efficiency, our experimental results clearly indicates that the overall surface area has no obvious effect on the photocatalytic degradation of organic dyes in the present study. The photocatalytic activity of as-prepared ferric giniite catalysts is highly dependent on the exposed facets, which is closely related to their preferential exposure of active iron atoms on the crystal surface. Our findings are helpful to understand and design new supported heterogeneous catalysts exposing uniformly high active sites with well-defined facets, thus presenting new opportunities for maximizing the photoreactivity through the morphological control of photocatalysts.

Results and Discussion

Structures and morphologies of the as-synthesized ferric giniite from [Bmim][H$_2$PO$_4$]/CH$_3$OH: The phase and purity of the as-obtained ferric giniite with different morphologies from the [Bmim][H$_2$PO$_4$]/CH$_3$OH were characterized by powder XRD measurements, as shown in Figure S1 (the Supporting Information). In all patterns, it is evident that all the diffraction peaks can be perfectly indexed to the orthorhombic structure of ferric giniite with lattice constants $a =$ 10.363 Å, $b = 26.072$ Å, $c = 5.175$ Å, which are consistent with the reported values (JCPDS Card 45-1436).[78] To further examine the representative morphologies and structures of as-synthesized ferric giniite from the [Bmim]-[H$_2$PO$_4$]/CH$_3$OH with different molar ratios of Fe-(NO$_3$)$_3$·9H$_2$O to [Bmim][H$_2$PO$_4$], SEM and TEM images were recorded, as shown in Figure 1. The micro-bipyramids with high quality crystalline and monodisperse are obtained when the molar ratio of n(Fe(NO$_3$)$_3$·9H$_2$O)/n([Bmim]-[H$_2$PO$_4$]) is 1:2 (S-1), which can be seen in Figure 1 A–D. Figure 1 A shows a typical large-area SEM image of the as-synthesized ferric giniite, indicating that the presence of homogeneous, well-shaped microcrystals with a size distribution ranging from 3.5 to 4.5 μm, with an average diameter of 4 μm. As shown in the high-magnification SEM image (Figure 1 B), the as-prepared simples are well-shaped polyhedra consisting of high-purity bipyramids with eight facets. Figure 1 C and D show the TEM image and the corresponding selected-area electron diffraction (SAED) pattern of a single ferric giniite bipyramid, respectively. The SAED pattern can be indexed to the [121] zone axis of single-crystal orthorhombic Fe$_5$(PO$_4$)$_4$(OH)$_3$·2H$_2$O, which indicates that the as-prepared ferric giniite bipyramids are single crystals enclosed by eight {111} facets. The ferric giniite microplates were obtained when the concentration of Fe(NO$_3$)$_3$·9H$_2$O increased to 3.33 mmol (S-2). Typical ferric giniite microplates are observed in SEM images and TEM images under different magnifications. Figure 1 E shows a low-magnification SEM image of the sample, which is composed of monodispersed large-scale microplates. From the high-magnification SEM image (Figure 1 F) and TEM image (Figure 1 G), we can see the individual ferric giniite micro-plate is micro-sized with a length of 3 μm and a thickness of 400 nm. The
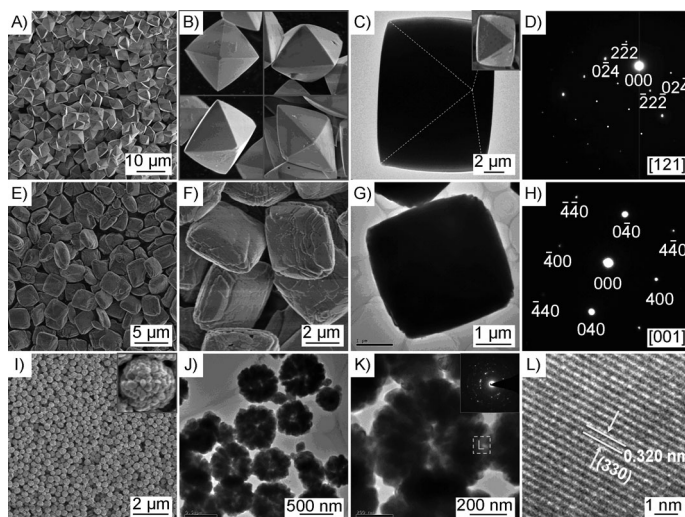
Figure 1. Representative morphologies and structures of as-synthesized ferric giniite from the [Bmim][H$_2$PO$_4$]/CH$_3$OH with different molar ratios of Fe(NO$_3$)$_3$·9H$_2$O to [Bmim][H$_2$PO$_4$]. A)–D) S-1 micro-bipyramids, when n(Fe(NO$_3$)$_3$·9H$_2$O)/n([Bmim][H$_2$PO$_4$]) = 1:2; A) Low-magnification SEM images of S-1; B) typical SEM images of S-1 from the different orientations; C) typical TEM image, and D) corresponding SAED pattern of S-1 viewed along the [121] direction, the inset of panel C is the corresponding SEM image. E–H) S-2, microplates, when n(Fe-(NO$_3$)$_3$·9H$_2$O)/n([Bmim][H$_2$PO$_4$]) = 1:1.5; E) low- and F) high-magnification SEM images of S-2, respectively; G) typical TEM image and H) corresponding SAED pattern of S-2 viewed along the [001] direction. I–L) S-3, hollow nanospheres, when n(Fe(NO$_3$)$_3$·9H$_2$O)/n([Bmim]-[H$_2$PO$_4$]) = 1:1; I) low magnification SEM images of S-1, the inset shows a typical individual nanosphere with a diameter of 500 nm, which is actually composed of hundreds of nanoparticles; J) low-, K) high-magnification TEM images and L) corresponding HRTEM image of S-3, respectively.

corresponding SAED pattern (Figure 1 H) shows that the diffraction spots are projected by the (400), (040), (440) planes and their equivalent surfaces under an incident electron beam along [001], which indicates that the as-prepared ferric giniite microplates are single crystals enclosed with {001} planes. When increasing the amount of Fe(NO$_3$)$_3$·9H$_2$O to change the molar ratio of n(Fe(NO$_3$)$_3$·9H$_2$O)/n([Bmim]-[H$_2$PO$_4$]) to 1:2 (S-3), the ferric giniite nanospheres are obtained. The low-magnification SEM images of the sample (Figure 1 I and the Supporting Information, Figure S2 A and B) indicate that the product is composed of monodispersed large-scale nanospheres. The inset of Figure 1 I shows a typical individual nanosphere with a diameter of 500 nm, exhibiting the detailed structural information of the nanospheres. The peripheral of the nanosphere is not smooth; it is actually composed of hundreds of nanoparticles with a size of about 50 nm. TEM and HRTEM were employed to further reveal the formation of the nanospheres. A hole is observed clearly in the center of the microsphere (Figure 1 J), which provides direct evidence that the ferric giniite nanospheres have a hollow structure composed of numerous tiny nanocrystals. From the high-magnification TEM image of a typical hollow nanosphere (Figure 1 K), it is obvious that the shell thickness of ferric giniite nanospheres is about 200 nm,

and the diameter of the hollow interiors is estimated to be about 100 nm. The corresponding HRTEM image (Figure 1 L) is taken at the edge of the nanosphere; by using this image, the clear lattice fringes and the interplane distances can be calculated as 0.32 nm, which corresponds to the (330) crystal planes of orthorhombic $Fe_5(PO_4)_4(OH)_3\cdot2H_2O$.

Structures and morphologies of as-synthesized ferric giniite from [Bmim][H$_2$PO$_4$]/CH$_3$OH/ethylene glycol (EG): When changing the ionic-liquid precursor mixtures to [Bmim]-[H$_2$PO$_4$]/CH$_3$OH/EG (V(CH$_3$OH)/V(EG)=1:2), and keeping the molar ratio of Fe(NO$_3$)$_3$·9H$_2$O to [Bmim][H$_2$PO$_4$] constant at 1:2, the ferric giniite tetragonal hexadecahedra are obtained (Figure 2). All of the diffraction peaks in the
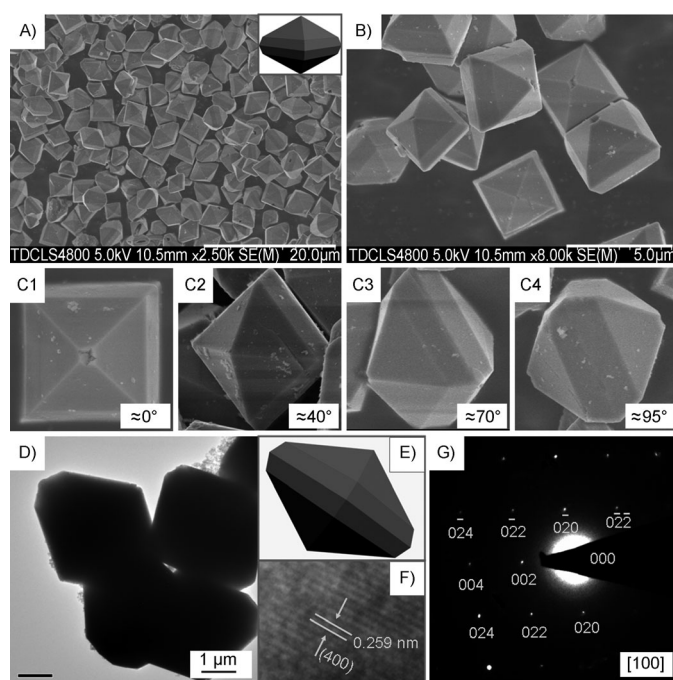
Figure 2. Representative morphologies and structures of as-synthesized ferric giniite from the [Bmim][H$_2$PO$_4$]/CH$_3$OH/EG. A) Low- and B) high-magnification SEM images of S-4, Fe$_5$(PO$_4$)$_4$(OH)$_3$·2H$_2$O micro-tetragonal hexadecahedra; C) SEM images of individual polyhedron in different orientations; D) Low-magnification and F) corresponding HRTEM images of S-4; E) related 3D model of tetragonal hexadecahedron; G) corresponding SAED pattern of the polyhedron under the incident electron beam along the [100] direction.

XRD patterns (the Supporting Information, Figure S3) of the obtained Fe$_5$(PO$_4$)$_4$(OH)$_3$·2H$_2$O samples can be indexed to the orthorhombic structure of ferric giniite (JCPDS Card 45-1436). Figure 2 A shows a typical large-area SEM image of the as-synthesized ferric giniite; nearly all of the samples are of well-shaped monodispersed microcrystals. As shown in the high-magnification SEM image (Figure 2 B and C), the as-prepared samples are well-shaped polyhedra comprising eight triangles and eight trapezoids, and are, thus, hexadecahedral. This tetragonal hexadecahedron has a four-fold axis and has a shape that is rarely observed for nanocrystals.

The TEM image of the obtained sample displayed polyhedron-like structures with a uniform size of around 3 μm. From the corresponding HRTEM image (Figure 2 F), it can be seen the clear lattice fringes and the interplane distances are calculated as 0.259 nm, corresponding to the (400) crystal planes of orthorhombic Fe$_5$(PO$_4$)$_4$(OH)$_3$·2H$_2$O, which indicates that the tetragonal hexadecahedron can be indexed to the [100] zone axis of a single ferric giniite crystal. In Figure 2 E and Figure S4 A (the Supporting Information), the corresponding geometrical model of the ideal hexadecahedron has been presented, which is in agreement with the as-prepared microcrystals (the Supporting Information, Figure S4 B and C). The exposed planes could be indexed to (111), (11−1), (−11−1), (−111), and (441), (44−1), (−44−1), and (−441). The angle between (111) plane and (441) plane of the as-prepared hexadecahedron is 144°, which is consistent with the simulation of the crystal structure value. Similar conclusions could be obtained from the SAED pattern in Figure 2 G, which can be indexed to the [100] zone axis of single-crystal orthorhombic Fe$_5$-(PO$_4$)$_4$(OH)$_3$·2H$_2$O.

Structures and morphologies of the as-synthesized ferric giniite from [Bmim][H$_2$PO$_4$]/CH$_3$OH/C$_4$H$_9$OH: When C$_4$H$_9$OH was added instead of EG (V(CH$_3$OH)/V-(C$_4$H$_9$OH)=1:2) under otherwise identical conditions, ferric giniite-truncated bipyramids with carved faces were obtained (Figure 3). All of the diffraction peaks in the XRD patterns (the Supporting Information, Figure S5) of the obtained Fe$_5$(PO$_4$)$_4$(OH)$_3$·2H$_2$O samples at different reaction times can be indexed to the orthorhombic structure of ferric giniite (JCPDS Card 45-1436). Figure 3 A and B show the typical SEM images of the ferric giniite-truncated bipyramids with carved faces in different orientations. From the top view (Figure 3 A), the truncated bipyramids are well-shaped and monodisperse with a uniform size of around 3 μm. It is clearly can be seen the central part of the top surface is almost empty and complete along the *c* axis. Further structural information for the truncated bipyramids with carved faces was provided by TEM. Figure 3 C shows the TEM image and corresponding SAED pattern (inset) of the as-prepared sample, respectively. The SAED pattern can be indexed to the [001] zone axis of single crystal orthorhombic Fe$_5$(PO$_4$)$_4$(OH)$_3$·2H$_2$O. To further confirm the exposed surfaces of the orthorhombic ferric giniite, the same sample was rotated to the [110] zone axis. The corresponding TEM image and SAED pattern can be seen in Figure 3 D. On the basis of the above TEM observations and structural analysis, it could be concluded that the exposed surfaces of the truncated bipyramids are {111} facets with selective etching along the *c* axis, leading to the formation of carved {001} faces. Figure 3 E shows the Scheme for the shape evolution from bipyramid to truncated bipyramid, concave bipyramid, and finally etching to a hollow structure. From the corresponding SEM images (Figure 3 F), it is visible that the process of face dissolution is not regular and starts from the top central parts of the bipyramid along the *c* axis.
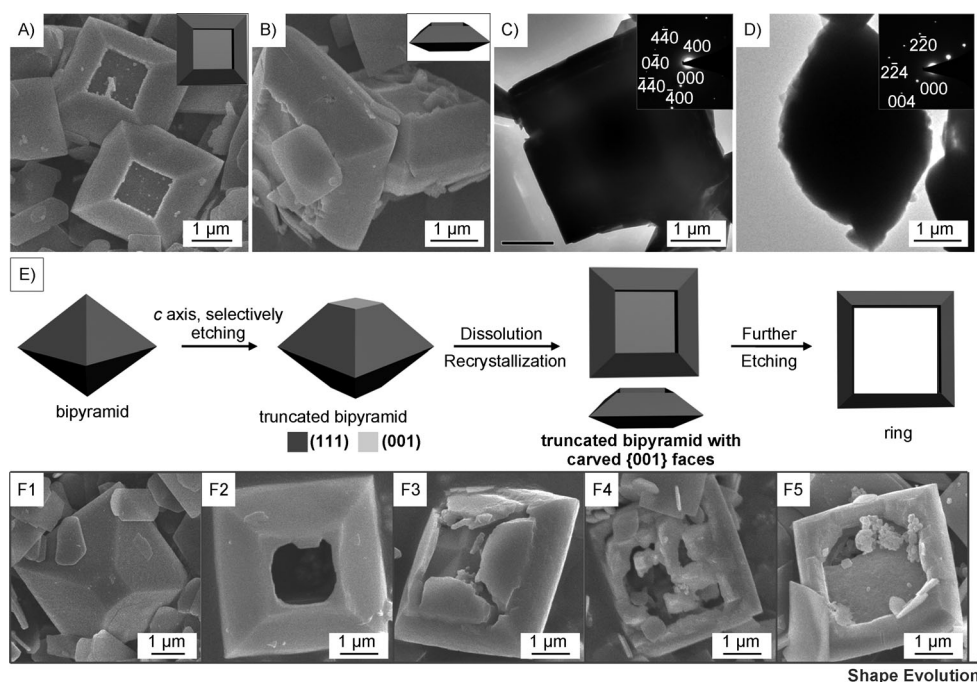
Figure 3. Representative morphologies and structures of as-synthesized ferric giniite ($Fe_5(PO_4)_4(OH)_3 \cdot 2H_2O$) from the [Bmim][$H_2PO_4$]/$CH_3OH$/$C_4H_9OH$. A and B) SEM images of S-6, truncated bipyramid ferric giniite with carved {001} faces in different orientations; C and D) Typical low-magnification TEM image of S-6, the insets are the corresponding SAED patterns viewed along the [001] and [110] directions, respectively; E) Scheme for the shape evolution of the concave polyhedron; F) The corresponding SEM images of the shape evolution in panel E.

Possible growth mechanism of ferric giniite crystals with various morphologies from the ionic-liquid precursors: *Formation of ferric giniite bipyramids, plates, and hollow spheres from [Bmim][H_2PO_4]/CH_3OH*: When using the ionic-liquid precursor [Bmim][H_2PO_4]/CH_3OH as the phosphate source, it is worth nothing that the only difference among the different ferric giniite microstructures was the molar ratio of Fe-($NO_3)_3\cdot9H_2O$ to [Bmim][H_2PO_4]. This implies that the relative [Bmim][H_2PO_4] concentration (relative to the concentration of Fe($NO_3)_3\cdot9H_2O$) in the reaction system may play an important role in tuning the particle morphology. To investigate the effect of the ionic liquid [Bmim][H_2PO_4] on the formation of ferric giniite with various morphologies, two controlled experiments were carried out. In the first experiment, [Bmim][H_2PO_4] replaced by $NH_4H_2PO_4$, whereas the other experimental conditions remained the same. Figure S7 (the Supporting Information) shows SEM images of the products synthesized with the molar ratios between Fe-($NO_3)_3\cdot9H_2O$ and $NH_4H_2PO_4$ of 1:2, 1:1.5, and 1:1. In the different molar ratios, only the ferric giniite micro-aggregations were produced, and there were no monodisperse polyhedral particles in the product. Thus, an important conclusion can be drawn: the existence of [Bmim][H_2PO_4] must be the key to controlling the polyhedral particle shape.

For elucidating the exact role played by [Bmim][H_2PO_4] in the synthesis of the ferric giniite, the other experiment was carried out in the different molar ratios between Fe-($NO_3)_3\cdot9H_2O$ and [Bmim][H_2PO_4]. Clearly, it can be seen that relatively high [Bmim][H_2PO_4] concentration favored

anisotropic growth of ferric giniite, leading to the formation of bipyramids (n(Fe($NO_3)_3\cdot9H_2O$)/n([Bmim][H_2PO_4])$=1$:2) and microplates (n(Fe($NO_3)_3\cdot9H_2O$)/n([Bmim][H_2PO_4])$=$ 1:1.5), whereas a relatively low [Bmim][H_2PO_4] concentration favored the isotropic growth to form nanospheres (n(Fe($NO_3)_3\cdot9H_2O$)/n([Bmim][H_2PO_4])$=1$:1). In the synthesis, when Fe($NO_3)_3\cdot9H_2O$ is dissolved into [Bmim][H_2PO_4]/CH_3OH mixtures, a yellowish-green solution can be obtained. Upon heating the reaction medium up to a sufficiently high temperature, the reactants chemically transform into active atoms to form the ferric giniite nuclei, which can be formulated as:

$$5Fe^{3+} + 4H_2PO_4^- + 5H_2O \rightarrow Fe_5(PO_4)_4(OH)_3 \cdot 2H_2O + 11H^+ \quad (1)$$
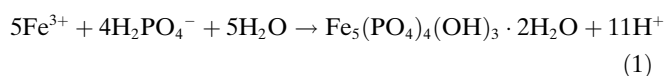
The subsequent growth is then greatly affected by the environmental media, which can affect the initial nuclei further growth and aggregation. Generally, the growth process of crystals can be separated into two steps, an initial nucleating stage and a subsequent crystal-growth process. At the initial nucleating stage, the crystalline phase of the seeds is critical for directing the intrinsic shapes of the crystals due to its characteristic symmetry and structure. At the subsequent step, the crystal-growth stage strongly governs the final architecture of the crystals through a delicate balance between the kinetic-growth and thermodynamic-growth regimes.[79–85] In the present study, we speculate that the final

ferric giniite microstructures are mainly determined by the molar ratios of $Fe(NO_3)_3 \cdot 9H_2O$ to $[Bmim][H_2PO_4]$; the Fe^{3+} concentration can affect the nucleation rate of ferric giniite and the $[Bmim]^+$ ions can stabilize the {111} facets of ferric giniite in the subsequent crystal-growth process.

With a low molar ratio of $Fe(NO_3)_3 \cdot 9H_2O$ to $[Bmim][H_2PO_4]$ (1:2), the low Fe^{3+} concentration results in lower ferric giniite nuclei concentration at the initial stage, which also means there are a large number of $[Bmim]^+$ ions could be selectively adsorbed on the crystal planes and affect the final morphology of ferric giniite. Compared with ferric giniite crystals in absence of $[Bmim]^+$ ions (the Supporting Information, Figure S7), the interactions between unprotected building units are generally not competent to form stable and uniform microstructures, confirming that the dispersibility of ferric giniite crystals is affected by $[Bmim]^+$ ions. The current results show that the ILs can be chosen to serve as stabilizers based on the selective adsorption of ILs on the surfaces of the samples. Therefore, in the work reported here, the presence of $[Bmim][H_2PO_4]$ was believed to play a strategic role on the formation of monodisperse bipyramids enclosed by {111} facets. As for ferric giniite, the habit of the orthorhombic crystal structure reveals that the {111} facets have higher energy than that of the {100} facets and {001} facets, due to higher packing density and the larger number of under-coordinated atoms.[84,85] To minimize the energy of the reaction system, the $[Bmim]^+$ ions could selectively passivate the {111} facets and hinder the growth of ferric giniite crystal along the <111> direction ($G_{<111>} < G_{<001>}$, $G_{<111>}$ represent that the growth rate is along the <111> direction). We and others have demonstrated the synthesis of nanostructures by ionic-liquid-assisted route,

and the electrostatic-attraction mechanism is helpful to understand the influence of ionic liquids on the size control of nanostructures.[82–84] It is assumed that the stabilization in these cases is essentially due to electrostatic attraction, which is induced by the adsorption of ILs on to the nanostructure surface, similar to the classic Dergaugin–Landau–Verwey–Overbeek (DLVO)-type coulombic repulsion model. Along with the $H_2PO_4^-$, $[Bmim]^+$ will also adsorb on the ferric giniite crystal surfaces possibly driven by the electrostatic attractions between $[Bmim]^+$ and $H_2PO_4^-$ (Scheme 1). As a result, $[Bmim]^+$ ions have a large steric hindrance, which would hinder the agglomeration of the obtained ferric giniite bipyramids in the solution and accordingly, the dispersibility of ferric giniite bipyramids with {111} facets terminated can be improved. To shed light on the adsorption of $[Bmim]^+$ ions on the ferric giniite surfaces, the as-prepared ferric giniite bipyramids were analyzed by using FT-IR spectroscopy (shown in Figure S8, the Supporting Information). When $[Bmim]^+$ ions are immobilized on to ferric giniite crystals, the peak of the hydroxyl groups of ferric giniite becomes broader, indicating a strong interaction between $[Bmim]^+$ ions and the ferric giniite surface. In addition, the absorption bands at 1570, 1163 and 758 cm^{-1} in Figure S8b (the Supporting Information), which was assigned to the skeleton stretching vibration of the imidazole ring, can also indicate strong interactions between $[Bmim]^+$ ions and the ferric giniite surface. Furthermore, the results of C and N elemental analysis display that no $[Bmim]^+$ ion clearly resides in the samples after washing several times with distilled water and anhydrous alcohol.

It should be pointed out that for protecting {111} facets the critical molar ratio of $[Bmim][H_2PO_4]$ to $Fe(NO_3)_3 \cdot 9H_2O$
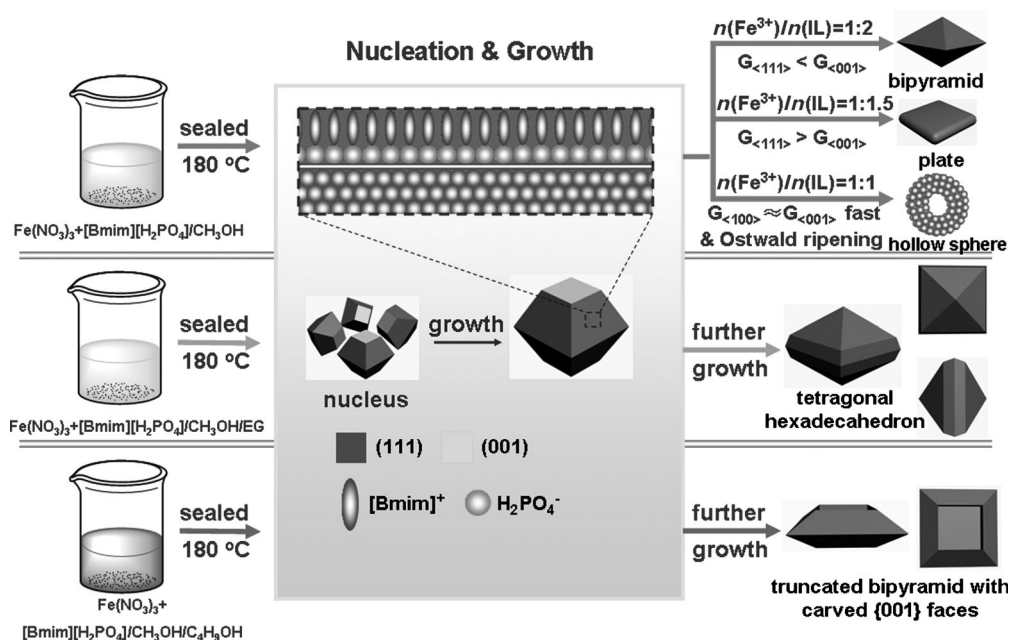
Scheme 1. Schematic illustration of the formations of ferric giniite crystals with various morphologies from ionic-liquid precursor: All the crystals were formed originally from the truncated bipyramid seeds. The formation of different morphologies were mainly attributed to the differences in the growth rate of the ferric giniite seeds under the assistance of strong adsorption of $[Bmim]^+$ ions on the {111} facets.

is 2. With an increased amount of $Fe(NO_3)_3\cdot9H_2O$ (S-2, 3.3 mmol) and with a molar ratio less than 2 (n([Bmim]-[H_2PO_4])/n(Fe(NO_3)_3\cdot9H_2O) = 1.5:1), ferric giniite micro-plate enclosed {001} facets can be obtained and no obvious effect of [Bmim]$^+$ ions was found on the formation of the ferric giniite bipyramid in protecting {111} facets. This result strongly indicated that there were a large number of nuclei in the initial reaction stage with increasing Fe^{3+} concentration, and no sufficient [Bmim]$^+$ ions in the system to protect the nuclei growth in the subsequent step. Thus, the assembly of microplates and the 2D growth behavior can be explained by the crystal nature and the growth situations of ortho-rhombic ferric giniite, because the {001} facets have the most low energy ({111} > {100} > {001}) and are the most stable planes of the ferric giniite crystal. According to Cornell and Schwertmann, low-energy planes tend to grow more slowly. The fast-growing {111} facets are eliminated quite rapidly, and therefore the slow-growing {001} facets determine the final morphology of ferric giniite plate. When increasing the amount of $Fe(NO_3)_3\cdot9H_2O$ to 5 mmol (n-([Bmim][H_2PO_4])/n(Fe(NO_3)_3\cdot9H_2O) = 1:1), ferric giniite hollow nanospheres (S-3) could be obtained, which may represent a new example of Ostwald ripening mechanism-based formation of inorganic hollow structures since the application of the Ostwald-ripening mechanism was proposed for the first time in the synthesis of TiO_2 hollow nanospheres reported by Zeng et al.[86–88] As is well-known, progressive nucleation would occur at higher Fe^{3+} supersaturation. When the nucleation rate is faster than the growth rate, the average crystal size can be decreased. Due to reduce surface-to-volume ratio and thus the surface energy, the initial ferric giniite nuclei aggregated in self-assembly and quickly became spherical in structure, because a sphere possesses the highest degree of symmetry compared with other possible geometric structures. Owing to the very fast nucleation, the aggregation process could be within a very short period of reaction time. In this process, nanoparticles located in the central part of the aggregate were believed to be smaller, as the nanoparticles in the shell were growing at the same time. Because of the size difference of the forming nanocrystals, previous studies have demonstrated that the Ostwald ripening process will happen during this time because smaller, less-crystalline, or less-dense particles in a colloidal aggregate will be dissolved gradually, while the larger, better crystallized, or denser particles in the same aggregate grow. Once the cores in the center of the nanospheres are consumed partially, the ferric giniite hollow nanospheres are formed.

Formation of ferric giniite tetragonal hexadecahedra from [Bmim][H_2PO_4]/CH_3OH/EG and carved truncated bipyramids from [Bmim][H_2PO_4]/CH_3OH/C_4H_9OH: It is interesting to note that ferric giniite tetragonal hexadecahedra (S-4) and carved polyhedra (S-6) can be obtained by adjusting the solvent composition of ionic-liquid precursor under a relatively high concentration of [Bmim][H_2PO_4]. According to the previous analysis, [Bmim]$^+$ ions played an essential role

in stabilizing the {111} facets of ferric giniite crystals when the molar ratio of [Bmim][H_2PO_4] to $Fe(NO_3)_3\cdot9H_2O$ is 2:1, which favors the formation of the final ferric giniite micro-crystals with a large percentage of active {111} facets. So, the formation of tetragonal hexadecahedra and carved polyhedra could be the result of a cooperative effect between [Bmim]$^+$ ions and additives (EG and C_4H_9OH).

Adjusting the ionic-liquid precursor mixtures to [Bmim]-[H_2PO_4]/CH_3OH/EG (V(CH_3OH)/V(EG) = 1:2) with other conditions unchanged, a remarkable transition occurred from ferric giniite bipyramids enclosed by {111} facets into tetragonal hexadecahedra (S-4) enclosed by {441} facets and {111} facets. This result demonstrated that EG contributed to stabilizing the high-index {441} facets of ferric giniite crystals. As is well-known, EG is often employed as a stabilizing agent in the polyol process, which can promote reduction onto specific crystal faces while preventing reduction on to others. In this present study, progressive nucleation would occur in the presence of EG owing to high reactivity; such high superaturation can easily result in high-speed growth of ferric giniite nuclei. Such post growth would be largely controlled by the kinetic parameters, which is based on manipulation of growth rate at which atoms are generated and added to the surface of a growing seed. As reported, kinetic control is most successful in generating nanocrystals that are enclosed by a concave surface and high-energy facets, with typical examples including truncated ditetragonal prisms enclosed by {310} facets,[91] trisoctahedra enclosed by {221} facets,[16] and tetrahexahedra enclosed by {730}, {210}, and {520} facets.[15] Although the actual mechanism for the selectivity is still under consideration, it is still believed that EG played a crucial role to stabilize the high-index {441} facets of ferric giniite crystals on the basis of above analysis, thus favoring the formation of the final tetragonal hexadecahedra under the assistance of the strong adsorption of [Bmim]$^+$ ions on the {111} facets. It is interesting to find that selective etching of hollow hexadecahedra of {441} facets could be achieved by prolonging the reaction time to 48 h (Figure 4), which could be attributed to the {441} facets having high energy, thus dissolution could occur with prolonged reaction time. By increasing the amount of $Fe(NO_3)_3\cdot9H_2O$ to 5 mmol, ferric giniite nanospheres could also be obtained (the Supporting Information, Figure S10), which is similar to the trend in [Bmim][H_2PO_4]/CH_3OH. The increased diameters of nanospheres (from 500 nm to 1 μm) also indicate that there could be a high nucleation rate and rapid aggregation process in the presence of EG. However, iron phosphate ($Fe_7(PO_4)_6$) containing a small amount of ferrous instead of ferric giniite could be obtained in [Bmim][H_2PO_4]/EG (the Supporting Information, Figure S11), owing to the weak reduction of EG toward Fe^{3+} in the solvothermal process. Varying the molar ratio of $Fe(NO_3)_3\cdot9H_2O$ to [Bmim]-[H_2PO_4], a morphology evolution from lotus-leaf-like (1:8, the Supporting Information, Figure S12), rugby-like (1:4, Figures S13 A and B in the Supporting Information,), and spindle-like (1:2, Figure S13 C, and 1:1.3, Figure S13 D in the Supporting Information) iron phosphate microstructures
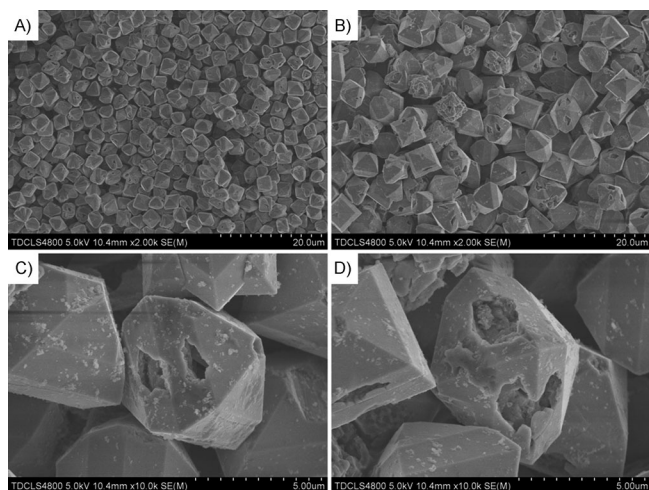
Figure 4. A), B) Low- and C), D) high-magnification SEM images of hollow $Fe_5(PO_4)_4(OH)_3 \cdot 2H_2O$ hexadecahedra, indicating that high-energy {441} facets could be selectively etched with prolonging the reaction time to 48 h.

were achieved, indicating that the concentration of [Bmim]-[H_2PO_4] played an important role in the formation of iron phosphate microstructures with different aspect ratios.

When C_4H_9OH was employed into the ionic-liquid precursor, [Bmim][H_2PO_4]/CH_3OH/C_4H_9OH (V(CH_3OH)/V-(C_4H_9OH)=1:1), ferric giniite-truncated bipyramids with carved {001} facets (S-6) were obtained. From the SEM images of the products taken at the prolonged reaction time (Figure 3F), it can be seen that the carved polyhedra undergo an evolution from truncated bipyramids into carved bipyramids and then into rings, which can be divided into two stages: formation of truncated bipyramids and then preferential dissolution along the c axis to form carved {001} facets. Structurally, C_4H_9OH contains four spatially symmetric hydroxyls. The introduction of this weakly polar solvent might reduce the adsorption of [Bmim]$^+$ ions on the ferric giniite crystal, thus weaken the protective effect of [Bmim]$^+$ ions on {111} facets, resulting in the formation of truncated bipyramids enclosed by {111} facets and {001} facets. This is consistent with the previous results on the formation of bipyramids in [Bmim][H_2PO_4]/CH_3OH. Taking into account the acidic reaction medium and H$^+$ ions produced by Equation (1) with prolonged reaction time, the ferric giniite microcrystals may begin to dissolve at a high reaction temperature. The dissolution occurs along the [001] direction, as the {001} facets are almost entirely exposed to solution without protection. The bipyramid surfaces are effectively protected by the adsorption of [Bmim]$^+$ ions on {111} facets. Therefore, the formation of carved bipyramid occurs through a process of preferential dissolution along the c axis. Therefore, the formation of truncated bipyramids with carved {001} facets could be by a cooperative effect between [Bmim]$^+$ ions and C_4H_9OH. Overall, based on the previous analysis, our proposed reaction mechanism in Scheme 1 is able to explain successfully the formation of ferric giniite

crystals with various morphologies from different ionic-liquid precursor.

Photocatalytic activity of ferric giniite crystals with various morphologies: Since ferric giniite tetragonal hexadecahedra (S-4) are exclusively enclosed by the active {441} and {111} facets, they may be expected to exhibit higher photoreactivity compared with normal ferric giniite crystals. To this end, their photocatalytic behaviors for the degradation of rhodamine B (RhB) and methyl blue (MB) dyes under visible-light irradiation were explored. For comparison, the performances of ferric giniite bipyramids enclosed by {111} facets (S-1), microplates enclosed by {001} facets (S-2), truncated bipyramids with carved {001} facets (S-6), and hollow nanospheres (S-3) were also investigated. Experimental conditions were adapted from the previous work so that the conditions would be optimal for photocatalytic comparisons among ferric giniite crystals with different morphologies.[50] As shown in Figure 5 A, it can be seen that all the ferric giniite photocatalysts showed little adsorption of RhB dye in dark and exhibited photocatalytic activities for the RhB degradation under visible-light irradiation. Compared with that observed in the dark, the photocatalytic activity in the presence of light is dramatically enhanced. Among them, the tetragonal hexadecahedra exhibited the highest photocatalytic activites, as they could completely degrade RhB dye in 120 min under visible-light irradiation. In contrast, the bipyramids, microplates and truncated bipyramids decomposed RhB dyes in ≈ 150, ≈ 180 and ≈ 240 min, respectively. Although the ferric giniite hollow nanospheres displayed more adsorption of RhB dye in the dark due to high surface areas (56.8 m^{2}g^{-1}), they has shown relatively lower photocatalytic activity under visible-light irradiation, which may attributed to their poor crystallinity and poorly defined crystal facets. It is well-known that a lot of defects could act as an electron-hole recombination center, resulting in a low photocatalytical activity. Taking into account the micron sizes of tetragonal hexadecahedron, bipyramid, plate and carved bipyramid, they had poor specific surface areas of 3.22 (S-4), 3.14 (S-1), 4.27 (S-2) and 2.54 (S-6) m^{2}g^{-1} by the Brunauer–Emment–Teller adsorption analysis, respectively. This result clearly indicates that the overall surface area has no obvious effect on the photocatalytic degradation of RhB in aqueous solution, which is consistent with previous literature reports.[32,53] On the basis of the above analysis, the significant difference in activities of ferric giniite catalysts should be attributed to their exposed facets. Additionally, the experimental results for the MB degradation with the same conditions clearly indicated that their photoactivity order has similar trend of the above results for the RhB degradation (Figure 5 B and the Supporting Information, Figure S14). This experiment reveals that the as-prepared ferric giniite catalysts are also efficient to degrade the dark-color organic molecule in aqueous solution. Comparing the degradation efficiency of ferric giniite with different shapes between RhB and MB under visible-light irradiation of 2 h (Figure 5 C), it is clear that the RhB dye is more easily decom-
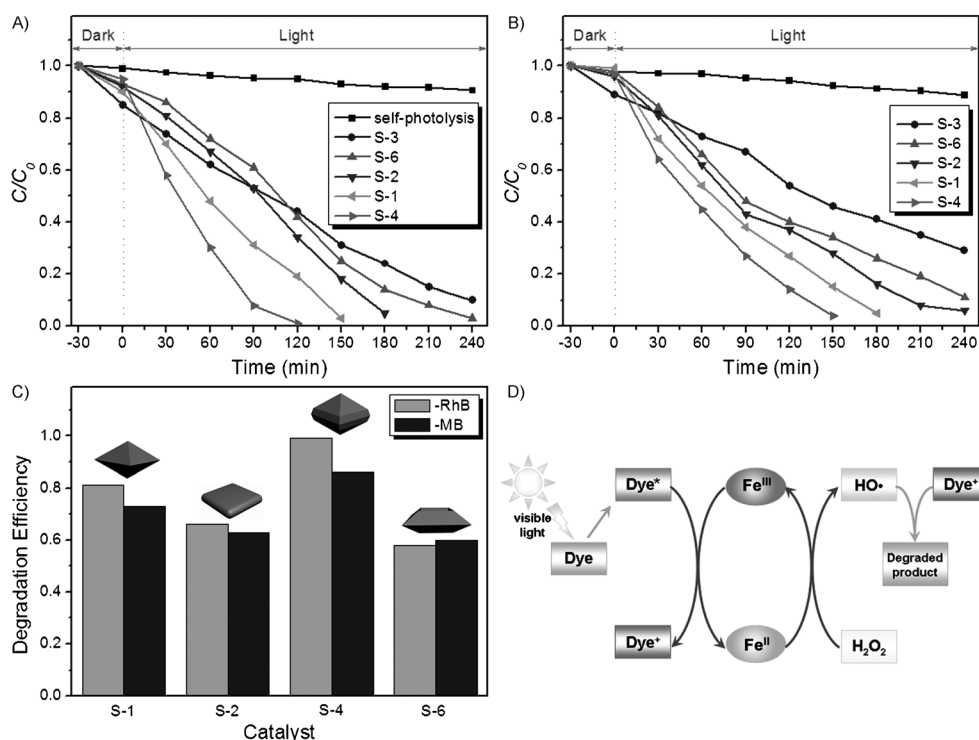
Figure 5. Photodegradation of RhB and MB on ferric giniite with different morphologies under visible-light irradiation ($\lambda > 420$ nm) in the presence of H_2O_2 additive: A) RhB and B) MB; C) photodegradation efficiency of ferric giniite with different shapes enclosed by different facets under visible-light irradiation of 2 h; D) scheme of the mechanism of the Fenton-like process with the assistance of visible-light irradiation.

posed, following the photoactivity order: tetragonal hexadecahedron > bipyramid > plate > carved bipyramid > hollow sphere. Therefore, these demonstrations indicate that the photocatalytic properties of ferric giniite crystals could be significantly improved by tailoring the shape and surface structure.

In the typical Fenton-like process involving the treatment of Fe^{II} with hydrogen peroxide, it can easily generate hydroxyl radicals as shown in Equation (2). This catalytic reaction is propagated by the reduction of Fe^{III} to Fe^{II} as shown in Equation (3), with the generation of more radicals as depicted by Equations (4) and (5).[43]

Dark :

$$Fe^{2+} + H_2O_2 \rightarrow Fe^{3+} + {}^{\cdot}OH + OH^-, \tag{2}$$
$$k_1 = 76\, \text{M}^{-1}\,\text{S}^{-1}$$

$$Fe^{3+} + H_2O_2 \rightarrow Fe^{2+} + {}^{\cdot}OOH + OH^-, \tag{3}$$
$$k_2 = 0.001 \approx 0.1\, \text{M}^{-1}\,\text{S}^{-1}$$

$$Fe^{3+} + {}^{\cdot}OOH \rightarrow Fe^{2+} + O_2 + H^+ \tag{4}$$

$$2{}^{\cdot}OOH \rightarrow O_2 + H_2O_2 \tag{5}$$

Light :

$$Dye + Vis.\, light \rightarrow Dye^* \tag{6}$$

$$Dye^* + Fe^{3+} \rightarrow Dye^+ + Fe^{2+} \tag{7}$$

$$Fe^{2+} + H_2O_2 \rightarrow Fe^{3+} + {}^{\cdot}OH + OH^- \tag{8}$$

$$Dye^+ + {}^{\cdot}OH \rightarrow products \tag{9}$$
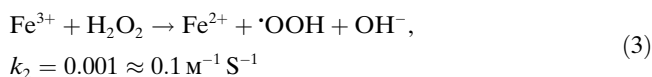
However, the reduction of Fe^{III} to Fe^{II} [Eq. (3)] is much slower than the decomposition of H_2O_2 in the presence of Fe^{II}. Thus, it is difficult to generate hydroxyl radicals for the degradation of organic dyes in the dark. On the contrary, an effective electron-transfer from the visible-light excited dyes* to Fe^{III} can be found, leading to regeneration of Fe^{II} and an easy cycle between Fe^{III} and Fe^{II}. With the assistance of an electron-transfer process, much faster degradation and mineralization of various dyes was achieved in the Fenton-like reaction under visible-light irradiation, as depicted by Equations (6)–(9). Apparently, to improve the photocatalytic performance, one must maximize the realization of electronic transfer from the excited dye* to Fe^{III}. According to previous reports, it is generally accepted that the coordinatively unsaturated iron cations, rather than bulk iron cations octahedrally coordinated by six oxygen anions, can offer catalytically active sites for dye* adsorbates. Given that the catalytic activity is highly dependent on the surface of active sites, a desirable goal for catalyst design and synthesis would be to decrease the less-reactive facets and increase the more-reactive facets so as to optimize the structure of the active sites. Thus, it can be easily understood that ferric gini-

ite tetragonal hexadecahedra enclosed by high-index facets exhibit better photocatalytic activity than the ones enclosed by low-index facets. Because it is conventionally considered that the high-index facets have a high percentage of low-co-ordinated atoms situated on the steps and kinks, with high reactivity required for high catalytic activity. Particularly, there are short-range steric sites that serve as catalytically active sites. Correspondingly, the observed photoreactivity of ferric giniite catalysts are a direct consequence of the active sites on the surface, with a reactivity order following: {441} > {111} > {001} facets. These results provide another good example that acquiring a high percentage of reactive facets by crystal-facet engineering is highly desirable for improving the photocatalytic reactivity.

Conclusion

We have successfully prepared ferric giniite crystals with controlled sizes and shapes, including bipyramids, plates, hollow spheres, tetragonal hexadecahedra, and carved bipyramids, in high purity by adjusting the concentration and composition of the ionic-liquid precursors. [Bmim][H$_2$PO$_4$] was found to play an important role in the evolution of ferric giniite crystals with different shapes, whereas [Bmim]$^+$ ions can favorably stabilize the {111} facets. Moreover, we systematically studied the photodegradation of RhB and MB these ferric giniite microstructures as Fenton-like catalysts. After comparing the catalytic performance of these ferric giniite crystals, we can conclude that the tetragonal hexadecahedra enclosed by {441} and {111} facets have the highest catalytic efficiency, which indicates that the photocatalytic activity of the as-prepared Fenton-like catalysts is highly dependent on the exposed facets. We believe this correlation between the catalytic activity and exposed facets will contribute to the rational design of Fenton-like catalysts with high efficiency.

Experimental Section

Materials: 1-n-Butyl-3-methy-limidazolium dihydrogenphosphate ([Bmim][H$_2$PO$_4$]) was obtained from Lanzhou Greenchem ILS, LICP. CAS. China. Other chemicals were purchased and used without further purification. The water was deionized before use.

Synthesis of ferric giniite micro-bipyramids: In a typical synthesis, [Bmim][H$_2$PO$_4$] (5 mmol; 1.18 g) was put into methanol (15 mL) under stirring to form a homogenous solution. Subsequently, Fe(NO$_3$)$_3$·9H$_2$O (2.5 mmol, 1.01 g) was added into the above homogenous solution under continuous stirring. Hydrochloric acid (HCl, 10 M) was added dropwise until the pH value of the mixture reached 2. After stirring for 10 min, the total solution was transferred into a stainless-steel autoclave with a capacity of 20 mL, sealed and heated at 180 °C for 12 h. When the reaction was complete, the autoclave was cooled to room temperature naturally. The resultant product was collected and washed with deionized water, and anhydrous ethanol for several times until the solution was neutral. The final product was dried in a vacuum at 80 °C for 3 h. Varying the amount of Fe(NO$_3$)$_3$·9H$_2$O and the composition of the solvent could produce a series of ferric giniite (Fe$_5$(PO$_4$)$_4$(OH)$_3$·2H$_2$O) with different sizes and morphologies. For investigation of the effect of ionic liquid [Bmim]-

[H$_2$PO$_4$], it was replaced by NH$_4$H$_2$PO$_4$, while preserving all the other conditions described above. The synthetic conditions for preparing some typical samples are summarized in Table S1 (the Supporting Information).

Photocatalysis measurements: Rhodamine B (RhB) and methyl blue (MB) dyes were selected to investigate the photocatalytic degradation of the as-prepared ferric giniite microcrystals. The batch experiment was first conducted in the dark. The photocatalyst (50 mg) was mixed with PhB (100 mL) or MB (0.01 mM) in a round-bottom flask (250 mL) under magnetic stirring. After 30 min in the dark to attain adsorption/desorption equilibrium, a solution of hydrogen peroxide (0.1 mL H$_2$O$_2$, 30 wt %) was added into the above suspension, followed by the irradiation of a 300 W xenon lamp. A cutoff filter of 420 nm was utilized to allow visible light to transmit, and a water filter was placed between the sample and the light source to maintain the working temperature and eliminate infrared irradiation. During the irradiation, the reaction suspension was magnetically stirred and kept at room temperature. At 30 min intervals, aliquots (about 5 mL) were sampled, centrifuged and filtered to remove the photocatalyst. The dye concentration in the filtrate was measured by UV spectra.

Characterization: The products were characterized by XRD, SEM, TEM, HR-TEM, SAED, FT-IR and BET measurements. XRD measurements were performed on a Rigaku D/max 2500 diffractometer with Cu$_{K\alpha}$ radiation ($\lambda = 0.154056$ nm) at $V = 40$ kV and $I = 150$ mA, and the scanning speed was 8° min^{-1}. Morphology observations were performed on a Hitachi S4800 field emission scanning electron microscope (FE-SEM). TEM, HR-TEM images and corresponding SAED patterns were recorded with a Tecnai G2 20S-Twin transmission electron microscope operating at an accelerating voltage of 120 kV. N$_2$ adsorption/desorption isotherms were collected at liquid nitrogen temperature using a Quantachrome Nova 2000e sorption analyzer. The specific surface areas (SBET) of the samples were calculated following the multipoint Brunauer–Emmett–Teller (BET) procedure. The FT-IR spectra of the samples were conducted at room temperature with a KBr pellet on a VECTOR-22 (Bruker) spectrometer ranging from 400 to 4000 cm^{-1}. The UV spectra of the dyes concentration at different time intervals were conducted by a Hitachi U-3900 UV/Vis spectrometer ranging from 400 to 800 nm.

[1] Valden, X. Lai, D. W. Goodman, *Science* **1998**, *281*, 1647–1650.

[2] K. B. Zhou, Y. D. Li, *Angew. Chem. Int. Ed.* **2012**, *51*, 602–613.

[3] T. Tachikawa, S. Yamashita, T. Majima, *J. Am. Chem. Soc.* **2011**, *133*, 7197–7204.

[4] Y. J. Xiong, Y. N. Xia, *Adv. Mater.* **2007**, *19*, 3385–3391.

[5] A. Tao, P. Sinsermsuksakul, P. D. Yang, *Angew. Chem.* **2006**, *118*, 4713–4717; *Angew. Chem. Int. Ed.* **2006**, *45*, 4597–4601.

[6] D. W. Goodman, *Chem. Rev.* **1995**, *95*, 523–536.

[7] G. Liu, J. C. Yu, G. Q. Lu, H. M. Cheng, *Chem. Commun.* **2011**, *47*, 6763–6783.

[8] S. E. Habas, H. Lee, V. Radmilovic, G. A. Somorjai, P. D. Yang, *Nat. Mater.* **2007**, *6*, 692–697.

[9] Z. Y. Zhou, N. Tian, J. T. Li, I. Broadwell, S. G. Sun, *Chem. Soc. Rev.* **2011**, *40*, 4167–4185.

[10] A. I. Hochbaum, P. D. Yang, *Chem. Rev.* **2010**, *110*, 527–546.

[11] S. W. Liu, J. G. Yu, M. Jaroniec, *J. Am. Chem. Soc.* **2010**, *132*, 11914–11916.

[12] J. S. Chen, Y. L. Tan, C. M. Li, Y. L. Cheah, D. Luan, S. Madhavi, F. Y. C. Boey, L. A. Archer, X. W. Lou, *J. Am. Chem. Soc.* **2010**, *132*, 6124–6130.

[13] H. Tong, S. X. Ouyang, Y. P. Bi, N. Umezawa, M. Oshikiri, J. H. Ye, *Adv. Mater.* **2012**, *24*, 229–251.

[14] Z. Y. Jiang, Q. Kuang, Z. X. Xie, L. S. Zheng, *Adv. Funct. Mater.* **2010**, *20*, 3634–3645.

[15] N. Tian, Z. Y. Zhou, S. G. Sun, Y. Ding, Z. L. Wang, *Science* **2007**, *316*, 732–735.

[16] Y. Y. Ma, Q. Kuang, Z. Y. Jiang, Z. X. Xie, R. B. Huang, L. S. Zheng, *Angew. Chem.* **2008**, *120*, 9033–9036; *Angew. Chem. Int. Ed.* **2008**, *47*, 8901–8904.

[17] Y. X. Chen, S. P. Chen, Z. Y. Zhou, N. Tian, Y. X. Jiang, S. G. Sun, Y. Ding, Z. L. Wang, *J. Am. Chem. Soc.* **2009**, *131*, 10860–10862.

[18] Z. Y. Zhou, Z. Z. Huang, D. J. Chen, Q. Wang, N. Tian, S. G. Sun, *Angew. Chem.* **2010**, *122*, 421–424; *Angew. Chem. Int. Ed.* **2010**, *49*, 411–414.

[19] T. Yu, D. Y. Kim, H. Zhang, Y. N. Xia, *Angew. Chem.* **2011**, *123*, 2825–2829; *Angew. Chem. Int. Ed.* **2011**, *50*, 2773–2777.

[20] T. Ming, W. Feng, Q. Tang, F. Wang, L. D. Sun, J. F. Wang, C. H. Yan, *J. Am. Chem. Soc.* **2009**, *131*, 16350–16351.

[21] J. Zhang, M. R. Langille, M. L. Personick, K. Zhang, S. Y. Li, C. A. Mirkin, *J. Am. Chem. Soc.* **2010**, *132*, 14012–14014.

[22] Y. Yu, Q. B. Zhang, B. Liu, J. Y. Lee, *J. Am. Chem. Soc.* **2010**, *132*, 18258–18265.

[23] X. Q. Huang, Z. P. Zhao, J. M. Fan, Y. M. Tan, N. F. Zheng, *J. Am. Chem. Soc.* **2011**, *133*, 4718–4721.

[24] Y. Q. Zheng, J. Tao, H. Y. Liu, J. Zeng, T. Yu, Y. Ma, C. Moran, L. J. Wu, Y. M. Zhu, J. Y. Liu, Y. N. Xia, *Small* **2011**, *7*, 2307–2312.

[25] X. H. Xia, J. Zeng, B. McDearmon, Y. Q. Zheng, Q. G. Li, Y. N. Xia, *Angew. Chem.* **2011**, *123*, 12750–12754.

[26] H. G. Yang, C. H. Sun, S. Z. Qiao, J. Zou, G. Liu, S. C. Smith, H. M. Cheng, G. Q. Lu, *Nature* **2008**, *453*, 638–641.

[27] H. G. Yang, G. Liu, S. Z. Qiao, C. H. Sun, Y. G. Jin, S. C. Smith, J. Zou, H. M. Cheng, G. Q. Lu, *J. Am. Chem. Soc.* **2009**, *131*, 4078–4083.

[28] X. G. Han, Q. Kuang, M. S. Jin, Z. X. Xie, L. S. Zheng, *J. Am. Chem. Soc.* **2009**, *131*, 3152–3153.

[29] G. Liu, H. G. Yang, X. W. Wang, L. N. Cheng, J. Pan, G. Q. Lu, H. M. Cheng, *J. Am. Chem. Soc.* **2009**, *131*, 12868–12869.

[30] H. Ariga, T. Taniike, H. Morikawa, M. Tada, B. K. Min, K. Watanabe, Y. Matsumoto, S. Ikeda, K. Saiki, Y. Iwasawa, *J. Am. Chem. Soc.* **2009**, *131*, 14670–14672.

[31] A. Y. Ahmed, T. A. Kandiel, T. Oekermann, D. Bahnemann, *J. Phys. Chem. Lett.* **2011**, *2*, 2461–2465.

[32] Y. P. Bi, S. X. Ouyang, N. Umezawa, J. Y. Cao, J. H. Ye, *J. Am. Chem. Soc.* **2011**, *133*, 6490–6492.

[33] W. C. Huang, L. M. Lyu, Y. C. Yang, M. H. Huang, *J. Am. Chem. Soc.* **2012**, *134*, 1261–1267.

[34] L. Q. Ye, L. Zan, L. H. Tian, T. Y. Peng, J. J. Zhang, *Chem. Commun.* **2011**, *47*, 6951–6953.

[35] J. Jiang, K. Zhao, X. Y. Xiao, L. Z. Zhang, *J. Am. Chem. Soc.* **2012**, *134*, 4473–4476.

[36] L. Q. Ye, L. Tian, T. Y. Peng, L. Zan, *J. Mater. Chem.* **2011**, *21*, 12479–12484.

[37] D. G. Wang, H. F. Jiang, H. Zong, Q. Xu, Y. Ma, G. L. Li, C. Li, *Chem. Eur. J.* **2011**, *17*, 1275–1282.

[38] C. C. Chen, W. H. Ma, J. C. Zhao, *Chem. Soc. Rev.* **2010**, *39*, 4206–4219.

[39] S. Navalon, R. Martin, M. Alvaro, H. Garcia, *Angew. Chem.* **2010**, *122*, 8581–8585.

[40] A. C. Yip, F. L. Lam, X. J. Hu, *Chem. Commun.* **2005**, *41*, 3218–3220.

[41] H. Lim, J. Lee, S. Jin, J. Kim, J. Yoon, T. Hyeon, *Chem. Commun.* **2006**, *42*, 463–465.

[42] G. Q. Zhang, S. Wang, F. L. Yang, *J. Phys. Chem. C* **2012**, *116*, 3623–3634.

[43] E. G. Garrido-Ramírez, B. K. G. Theng, M. L. Mora, *Appl. Clay Sci.* **2010**, *25*, 182–192.

[44] G. B. Ortizi de la Plata, O. M. Alfano, A. E. Cassano, *Appl. Catal. B* **2010**, *95*, 14–25.

[45] J. H. Deng, J. Y. Jiang, Y. Y. Zhang, X. P. Lin, C. M. Du, Y. Xiong, *Appl. Catal. B* **2008**, *84*, 468–473.

[46] L. Guo, F. Chen, X. Fan, W. Cai, J. Zhang, *Appl. Catal. B* **2010**, *96*, 162–168.

[47] M. Hartmann, S. Kullmann, H. Keller, *J. Mater. Chem.* **2010**, *20*, 9002–9017.

[48] G. Zhang, Y. Gao, L. Zhang, Y. Guo, *Environ. Sci. Technol.* **2010**, *44*, 6384–6389.

[49] J. K. Kim, F. Martinez, I. S. Metcalfe, *Catal. Today* **2007**, *124*, 224–231.

[50] D. Li, C. Pan, R. Shi, F. Zhu, *CrystEngComm* **2011**, *13*, 6688–6693.

[51] J. Ma, W. Ma, C. Chen, H. Ji, J. Zhao, *Chem. Asian J.* **2011**, *6*, 2264–2268.

[52] C. Sun, C. Chen, W. Ma, J. Zhao, *Phys. Chem. Chem. Phys.* **2011**, *13*, 1957–1969.

[53] X. Zhou, J. Lan, G. Liu, K. Deng, Y. Yang, G. Nie, J. Yu, L. Zhi, *Angew. Chem.* **2012**, *124*, 182–186.

[54] N. Recham, L. Dupont, M. Courty, K. Djellab, D. Larcher, M. Armand, J. M. Tarascon, *Chem. Mater.* **2009**, *21*, 1096–1107.

[55] Z. Ma, J. Yu, S. Dai, *Adv. Mater.* **2010**, *22*, 261–285.

[56] C. Zhang, J. Chen, X. Zhu, Y. Zhou, D. Li, *Chem. Mater.* **2009**, *21*, 3570–3575.

[57] J. Cybinska, C. Lorbeer, E. Zych, A. V. Mudring, *ChemSusChem* **2011**, *4*, 595–598.

[58] Z. Li, P. Rabu, P. Strauch, A. Mantion, A. Taubert, *Chem. Eur. J.* **2008**, *14*, 8409–8417.

[59] M. Armand, F. Endres, D. R. MacFarlane, H. Ohno, B. Scrosati, *Nat. Mater.* **2009**, *8*, 621–629.

[60] H. Zhu, J. Huang, Z. Pan, S. Dai, *Chem. Mater.* **2006**, *18*, 4473–4477.

[61] P. Migowski, D. Zanchet, G. Machado, M. A. Gelesky, S. R. Teixeira, J. Dupont, *Phys. Chem. Chem. Phys.* **2010**, *12*, 6826–6833.

[62] J. S. Lee, X. Q. Wang, H. M. Luo, G. A. Baker, S. Dai, *J. Am. Chem. Soc.* **2009**, *131*, 4596–4597.

[63] W. Yang, T. P. Fellinger, M. Antonietti, *J. Am. Chem. Soc.* **2011**, *133*, 206–209.

[64] W. Dobbs, J. Suisse, L. Douce, R. Welter, *Angew. Chem.* **2006**, *118*, 4285–4288.

[65] J. Lian, X. Duan, J. Ma, P. Peng, T. Kim, W. Zheng, *ACS Nano* **2009**, *3*, 3749–3761.

[66] H. S. Park, B. G. Choi, S. H. Yang, W. H. Shin, J. K. Kang, D. Jung, W. H. Hong, *Small* **2009**, *5*, 1754–1760.

[67] T. Torimoto, T. Tsuda, K. Okazaki, S. Kuwabata, *Adv. Mater.* **2010**, *22*, 1196–1221.

[68] T. Kim, W. Kim, S. Hong, J. Kim, K. Suh, *Angew. Chem.* **2009**, *121*, 3864–3867.

[69] M. Scariot, D. Silva, J. Scholten, G. Machado, S. Teixeira, M. Novak, G. Ebeling, J. Dupont, *Angew. Chem.* **2008**, *120*, 9215–9218; *Angew. Chem. Int. Ed.* **2008**, *47*, 9075–9078.

[70] X. Zhao, W. Jin, J. Cai, J. Ye, Z. Li, Y. Ma, J. Xie, L. Qi, *Adv. Funct. Mater.* **2011**, *21*, 3554–3563.

[71] Z. Li, A. Geßner, J. Richters, J. Kalden, T. Voss, C. Kübel, A. Taubert, *Adv. Mater.* **2008**, *20*, 1279–1285.

[72] J. P. Paraknowitsch, J. Zhang, D. Su, A. Thomas, M. Antonietti, *Adv. Mater.* **2010**, *22*, 87–92.

[73] H. Park, S. H. Yang, Y. S. Jun, W. H. Hong, J. K. Kang, *Chem. Mater.* **2007**, *19*, 535–542.

[74] H. S. Park, Y. S. Choi, Y. M. Jung, W. H. Hong, *J. Am. Chem. Soc.* **2008**, *130*, 845–852.

[75] M. He, P. Huang, C. Zhang, H. Hu, C. Bao, G. Gao, R. He, D. Cui, *Adv. Funct. Mater.* **2011**, *21*, 4470–4477.

[76] M. He, P. Huang, C. Zhang, J. Ma, R. He, D. Cui, *Chem. Eur. J.* **2012**, *18*, 5954–5969.

[77] T. Roncal-Herrero, J. D. Rodríguez-Blanco, L. G. Benning, E. H. Oelkers, *Cryst. Growth Des.* **2009**, *9*, 5197–5205.

[78] H. E. Buckley, *Crystal Growth*, Wiley, New York, **1951**.

[79] S. Mann, *Angew. Chem.* **2000**, *112*, 3532–3548.

[80] M. J. Siegfried, K. S. Choi, *Angew. Chem.* **2005**, *117*, 3282–3287.

[81] A. Tao, S. Habas, P. D. Yang, *Small* **2008**, *4*, 310–325.

[82] Y. Sun, Y. Xia, *Science* **2002**, *298*, 2176–2179.

[83] E. Greyson, J. Barton, T. Odom, *Small* **2006**, *2*, 368–371.

[84] D. Chen, L. Gao, A. Yasumori, K. Kuroda, Y. Sugahara, *Small* **2008**, *4*, 1813–1822.

[85] H. G. Yang, H. C. Zeng, *J. Phys. Chem. B* **2004**, *108*, 3492–3495.

[86] J. Li, H. C. Zeng, *J. Am. Chem. Soc.* **2007**, *129*, 15839–15847.

[87] H. C. Zeng, *J. Mater. Chem.* **2006**, *16*, 649–662.

[88] W. Zheng, X. Liu, Z. Yan, L. Zhu, *ACS Nano* **2009**, *3*, 115–122.

[89] X. Duan, J. Lian, J. Ma, T. Kim, W. Zheng, *Cryst. Growth Des.* **2010**, *10*, 4449–4455.

[90] X. Duan, X. Liu, Q. Chen, H. Li, J. Li, X. Hu, Y. Li, J. Ma, W. Zheng, *Dalton Trans.* **2011**, *40*, 1924–1928.

[91] F. Lu, Y. Zhang, L. Zhang, Y. Zhang, J. Wang, R. R. Adzic, E. A. Stach, O. Gang, *J. Am. Chem. Soc.* **2011**, *133*, 18074–18077.